Rapid Communications

Dynamical axion state with hidden pseudospin Chern numbers in $MnBi_2Te_4$-based heterostructures

Huaiqiang Wang,[1] Dinghui Wang,[1] Zhilong Yang,[1] Minji Shi,[1] Jiawei Ruan,[1] Dingyu Xing,[1,2] Jing Wang,[3,2,4,*] and Haijun Zhang[1,2,†]

[1]*National Laboratory of Solid State Microstructures, School of Physics, Nanjing University, Nanjing 210093, China*

[2]*Collaborative Innovation Center of Advanced Microstructures, Nanjing University, Nanjing 210093, China*

[3]*State Key Laboratory of Surface Physics, Department of Physics, Fudan University, Shanghai 200433, China*

[4]*Institute for Nanoelectronic Devices and Quantum Computing, Fudan University, Shanghai 200433, China*

(Received 9 November 2019; accepted 4 February 2020; published 24 February 2020)

An axion is a hypothetical elementary particle which was initially postulated to solve the charge conjugation-parity problem in particle physics. Interestingly, the axion state has emerged in the effective theory of topological insulators and has attracted extensive attention in condensed matter physics. Time-reversal or inversion symmetry constrains the axion field θ to be quantized. When both the time-reversal and inversion symmetries are broken by, say, an antiferromagnetic order, the axion field θ could become unquantized and dynamical along with magnetic fluctuations, which is termed the dynamical axion field. Here, we reveal that a wide class of topological-insulator-based dynamical axion states could be distinguished from the normal-insulator-based ones by a hidden quantity derived from the pseudospin Chern number. Motivated by recent research on the $MnBi_2Te_4$ family of materials, we further show that such topological-insulator-based dynamical axion states can be hopefully achieved in $MnBi_2Te_4$-based heterostructures, which should greatly facilitate the study of axion electrodynamics in condensed matter physics.

DOI: 10.1103/PhysRevB.101.081109

Introduction. Recently, many analogs of elementary particles, which were originally discovered in particle physics, have been found as quasiparticle excitations in condensed matter physics, such as, for example, the massless Weyl and Dirac fermions in topological semimetals [1] and mysterious Majorana fermions in topological superconductors [2,3]. Among them, the search for an axion state has attracted intensive interest in condensed matter physics [4–41]. As a hypothetical elementary particle, the axion is a possible component of dark matter of the Universe [42]. Axions gained new vigor from the effective theory of topological insulators (TIs) [2,4], which is described by an axion Lagrangian density $\mathcal{L}_\theta = (\theta/2\pi)(\alpha/2\pi)\mathbf{E}\cdot\mathbf{B}$. Here, $\alpha = e^2/\hbar c$ is the fine structure constant, $\mathbf{E}$ and $\mathbf{B}$ represent electric and magnetic fields, and the dimensionless pseudoscalar θ is a parameter describing the insulator, which is referred to as the axion field in axion electrodynamics [43]. Generically, θ is odd under time-reversal symmetry (TRS) and inversion symmetry (IS). With periodic boundary conditions in space-time, θ has a 2π periodicity and it is constrained to π for time-reversal-invariant TIs and 0 for normal insulators (NIs). Such quantized θ in TIs will lead to the topological magnetoelectric effect [4–9,11–13,44] and unique magneto-optical Faraday and Kerr effects [27,45–48].

Once both TRS and IS are broken, θ deviates from the quantized value of 0 or π, as has been shown for TIs in the presence of antiferromagnetic (AFM) order [49,50] and antiferromagnet chromia [51]. Intriguingly, an inherently fluctuating AFM order will induce fluctuations of the axion field θ as a dynamical variable with spatial and temporal dependence [11,49,50,52,53]. Such a dynamical axion field could give rise to rich, interesting effects, such as the dynamical chiral magnetic effect and anomalous Hall effect [43,54,55], instability in an external electric field [56,57], and axionic polaritons [49].

Up to now, two important issues on the dynamical axion state still remain open. First, since the broken TRS invalidates the Z_2 topological invariant in TIs [58], it remains unknown whether it is available to distinguish the TI-based dynamical axion state [49] with a large static $\theta \sim \pi$ from the NI-based one with a small static $\theta \sim 0$ [59]. Second, the experimental demonstration of a TI-based dynamical axion state is significantly hindered by the lack of realistic materials. Here, we explicitly address the above two issues in the affirmative. First, based on an effective model analysis, we uncover a hidden quantity derived from pseudospin Chern numbers [60–62] to differentiate a wide class of TI- and NI-based dynamical axion states. Further, inspired by recent studies on the $MnBi_2Te_4$ family of intrinsic magnetic insulators [24,25,35–37,63–68], we find that TI-based dynamical axion states can be hopefully achieved in $MnBi_2Te_4/Bi_2Te_3$-based magnetic van der Waals (vdW) heterostructures through breaking both TRS and IS by specific structural designs. Interestingly, some natural vdW heterostructures of $(MnBi_2Te_4)_m(Bi_2Te_3)_n$ have been experimentally fabricated [68–70], which may provide an ideal platform to study the axion electrodynamics and to detect the axion dark matter [71].

*wjingphys@fudan.edu.cn
†zhanghj@nju.edu.cn

Low-energy effective model. Without loss of generality, we start from the typical low-energy effective model of the Bi_2Te_3 family of TIs [72] and then treat the AFM order as a perturbation [49]. In the nonmagnetic state with the preserved IS, the four low-lying states are the bonding states $|P1_z^+, \uparrow(\downarrow)\rangle$ from Bi atoms and antibonding states $|P2_z^-, \uparrow(\downarrow)\rangle$ from Te atoms, where the superscript "+" ("−") represents positive (negative) parity. In the ordered basis of $(|P1_z^+, \uparrow\rangle, |P1_z^+, \downarrow\rangle, |P2_z^-, \uparrow\rangle, |P2_z^-, \downarrow\rangle)$, the symmetry operations of the D_{3d} group at Γ are represented, for example, as TRS $\mathcal{T} = \tau_0 \otimes i\sigma_y K$, IS $\mathcal{P} = \tau_z \otimes \sigma_0$, rotation symmetries $C_{3z} = \exp[\tau_0 \otimes (-i\pi/3)\sigma_z]$ and $C_{2x} = \exp[\tau_0 \otimes (-i\pi/2)\sigma_x]$, where K denotes the complex conjugate, τ_0 and σ_0 are 2×2 identity matrices, and $\tau_{x,y,z}$ and $\sigma_{x,y,z}$ are Pauli matrices acting in the orbital and spin spaces, respectively. Keeping the most relevant terms up to quadratic order of k, the effective four-band Hamiltonian is given by

$$\mathcal{H}_0(\mathbf{k}) = \epsilon_0(\mathbf{k})\mathbb{I}_{4\times4} + \sum_{i=1}^{5} d_i(k)\Gamma^i,$$
$$d_{1,2,\ldots,5}(\mathbf{k}) = [A_2k_y, -A_2k_x, A_1k_z, M(\mathbf{k}), 0], \quad (1)$$

where $\epsilon_0(\mathbf{k}) = C + D_1k_z^2 + D_2(k_x^2 + k_y^2)$, $M(\mathbf{k}) = M + B_1k_z^2 + B_2(k_x^2 + k_y^2)$, and the five Dirac matrices are represented as $\Gamma^{1,2,\ldots,5} = (\tau_x \otimes \sigma_x, \tau_x \otimes \sigma_y, \tau_y \otimes \sigma_0, \tau_z \otimes \sigma_0, \tau_x \otimes \sigma_z)$, which satisfy the Clifford algebra $\{\Gamma^i, \Gamma^j\} = 2\delta_{i,j}$. The TI phase requires the condition of $M/B_{i=1,2} < 0$. Hereafter, we assume $B_{i=1,2}$ to be positive, and $M < 0$ ($M > 0$) corresponds to the TI (NI).

The AFM order breaks both $\mathcal{P}$ and $\mathcal{T}$ simultaneously, which is essential for the emergence of dynamical axion states, and to the leading order, it will give rise to the $\mathcal{P}$- and $\mathcal{T}$-breaking mass term $\delta\mathcal{H}_{\rm AFM} = m_5\Gamma_5$ [49]. Furthermore, if the AFM order preserves the combined $\mathcal{PT}$ symmetry, only the identity matrix $\mathbb{I}_{4\times4}$ and the above five linearly independent anticommuting Dirac matrices $\Gamma^{1,2,\ldots,5}$ are allowed [73]. Consequently, the total Hamiltonian is written as $\mathcal{H}(\mathbf{k}) = \mathcal{H}_0(\mathbf{k}) + m_5\Gamma_5$, and the antiunitary $\mathcal{PT}$ symmetry with $(\mathcal{PT})^2 = -1$ ensures the double degeneracy of each band. It should be emphasized that due to the nonvanishing AFM mass term, when tuning M from negative (TI side) to positive (NI side), there will be no topological phase transition, but a crossover with an avoided gap closing. Nevertheless, the two magnetic states in the TI and NI sides, respectively, can still be differentiated by a hidden Z_2-like quantity derived from the pseudospin Chern numbers as we show below.

Pseudospin Chern number. The (pseudo)spin Chern number was originally proposed in the quantum spin Hall effect [60], which remains valid and robust even when TRS is broken or the (pseudo)spin is not conserved [60–62,74]. The definition of the pseudospin Chern number relies on a smooth decomposition of the occupied valence bands into two pseudospin sectors through projecting a pseudospin operator $\hat{S}$ into valence bands as $h_S = P_v\hat{S}P_v$ with P_v as the valence-band projecting operator [60–62,73]. Diagonalization of h_S then gives rise to two pseudospin branches with eigenvalues $\pm\epsilon_S(\mathbf{k})$, and corresponding eigenvectors $|\varphi_\pm\rangle$. For each pseudospin branch, the usual Chern number can be calculated in two-dimensional (2D) momentum space as

$$C_\pm^S = \frac{1}{2\pi}\int d^2k\Omega_\pm^{\mu\nu}, \quad (2)$$

where $\Omega_\pm^{\mu\nu} = -2\,\mathrm{Im}\langle\frac{\partial\varphi_\pm}{\partial k_\mu}|\frac{\partial\varphi_\pm}{\partial k_\nu}\rangle$ is the Berry curvature in the 2D k_μ-k_ν slice. The pseudospin Chern number is then defined as $C^S = (C_+^S - C_-^S)/2$.

By treating one momentum as a parameter, we can calculate C^S for each 2D slice in the 3D Brillouin zone. Specifically, we treat k_z as the parameter and investigate the 2D slices (k_x-k_y). We construct the pseudospin operator as $\hat{S} = \tau_z\sigma_z$ in the current basis of $\mathcal{H}(\mathbf{k})$ [73]. The k_z-dependent pseudospin Chern number can then be analytically derived as [73]

$$C^S(k_z) = \tfrac{1}{2}\big[-\mathrm{sgn}(B_2) + \mathrm{sgn}\big(M + B_1k_z^2\big)\big]. \quad (3)$$

Interestingly, it is independent of the AFM mass m_5. Since B_1 and B_2 are positive, $C^S(k_z)$ always equals zero in the NI-based regime with $M > 0$, whereas one can obtain $C^S(k_z) = -1$ for $|k_z| < k_{zc} = \sqrt{-M/B_1}$ and $C^S(k_z) = 0$ for $|k_z| > k_{zc}$ in the TI-based regime with $M < 0$, as shown in Fig. 1(a). It is noteworthy that the change of $C^S(k_z)$ here is accompanied by the closing of the pseudospin-spectrum gap instead of the energy gap which is always kept open. This can be seen by the k_z-dependent pseudospin spectrum ϵ_S at $(0, 0, k_z)$ in Fig. 1(a) with a closing point at $|k_z| = k_{zc}$. Representative pseudospin spectra in the k_x-k_y plane are also shown in Fig. 1(c) for $|k_z| < k_{zc}$ (left column), $|k_z| = k_{zc}$ (middle column), and $|k_z| > k_{zc}$ (right column), respectively. Moreover, we stress that the pseudospin Chern number remains quantized even though the pseudospin is not conserved for $k_z \neq 0$ (ϵ_S deviates from ±1) [61]. This can alternatively be reflected by the $U(1)$ Wilson loop spectra [75] for each pseudospin branch in the 2D slice ($k_x - k_y$) of a lattice model [73]. As shown in Fig. 1(b), when k_x goes from 0 to 2π, the Wilson loop of the lower pseudospin branch exhibits one (no) winding for $C_-^S(k_z) = +1(0)$.

In the TI-based magnetic state, such a change of C^S from $k_z = 0$ to $|k_z| > k_{zc}$ essentially results from the inverted band structure ($M < 0$) at the Γ point of the parent TI. This enables us to define a Z_2-like quantity ν as

$$\nu = (-1)^{C^S(k_z=0)+C^S(k_z=\infty)}, \quad (4)$$

where $k_z = \infty$ should be replaced by $k_z = \pi$ in Bloch bands, and $\nu = -1$ (or $+1$) corresponds to the TI-based (NI-based) state. It is worth mentioning that when treating k_x (or k_y) as a parameter, through similar procedures of calculating k_x- (or k_y-) dependent pseudospin Chern numbers [73], identical ν can be obtained. Strictly speaking, ν is not a topological invariant since the above two magnetic states are topologically the same with an avoided gap-closing crossover. Nonetheless, a "nontrivial" $\nu = -1$ still acts as a useful quantity which captures the band-inversion information of the parent TI state. Such a quantity can be applied to a wide class of 3D magnetic insulators, as long as the time-reversal-invariant 2D plane could be effectively reduced to a Bernevig-Hughes-Zhang-like model [76,77] by some unitary transformations without the TRS-breaking magnetic order.

Massive Dirac surface states. For a 3D TI, gapless surface states, with a single massless Dirac cone, emerge on the surface. However, due to the AFM mass term in

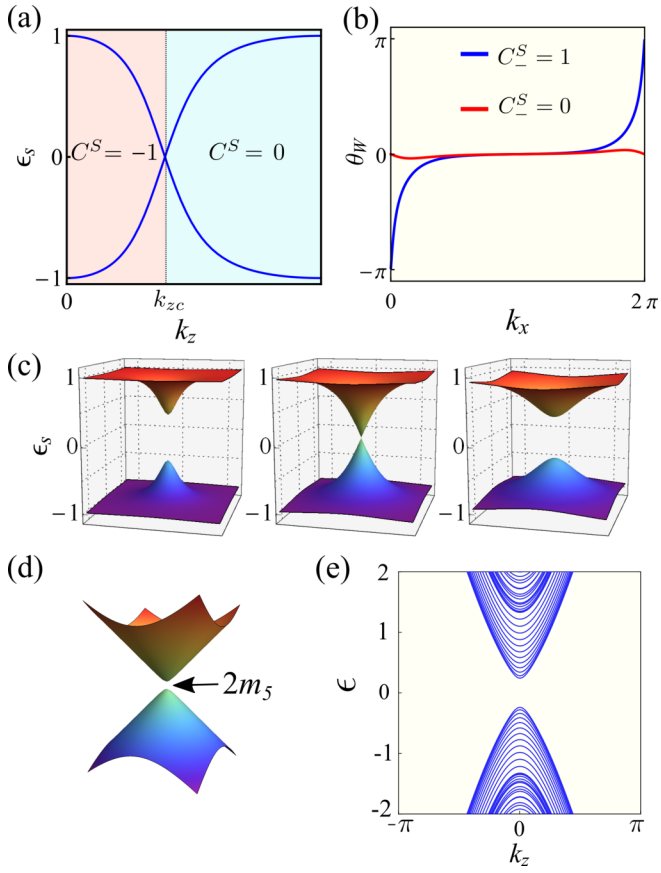

FIG. 1. (a) The k_z-dependent pseudospin spectrum at $k_x = k_y = 0$, with the gap closing at $k_{zc} = \sqrt{-M/B_1}$. (c) Three representative pseudospin spectra in the 2D slice (k_x-k_y) for $|k_z| < k_{zc}$ (left), $|k_z| = k_{zc}$ (middle), and $|k_z| > k_{zc}$ (right). (b) Representative $U(1)$ Wilson loops for the lower branch of the pseudospin spectra in the 2D slice (k_x-k_y) of a lattice model as a function of k_x when $C_-^S(k_z) = 1$ (blue line) and 0 (red line), respectively. (d) Schematic illustration of the massive Dirac surface state with a $2m_5$ gap inherited from the bulk bands. (e) Energy spectrum along the k_z direction with open-boundary conditions in both x and y directions. The parameters are typically chosen as $C = D_1 = D_2 = 0, A_1 = A_2 = B_1 = B_2 = 1$, $M = -0.3$, and $m_5 = 0.03$, which are given in dimensionless form for simplicity.

TI-based states, surface states are gapped with a single massive Dirac cone on all surfaces, which can be clearly seen by transforming the above continuum model to a tight-binding one on a cubic lattice. The massive Dirac-cone surface states along the z direction can be derived as $h^z_{\text{surf}} = \pm[A_2(k_y\sigma_x - k_x\sigma_y) + m_5\sigma_z]$ [73], where "+" and "−" refer to the bottom and top surfaces, respectively, indicating an energy gap of $2m_5$ for the surface bands, as shown in Fig. 1(d). Similarly, for the surface states along the x and y directions, the effective Hamiltonians are given by $h^x_{\text{surf}} = \mp(A_2k_y\sigma_z + A_1k_z\sigma_y + m_5\sigma_x)$ and $h^y_{\text{surf}} = \pm(-A_2k_x\sigma_z + A_1k_z\sigma_x - m_5\sigma_y)$, respectively [73]. Note that all surfaces are gapped for our model and that no one-dimensional gapless hinge states are found, as shown in Fig. 1(e) by the energy spectrum with open-boundary conditions in both the x and y directions. This is different from the recently proposed (static) axion insulators

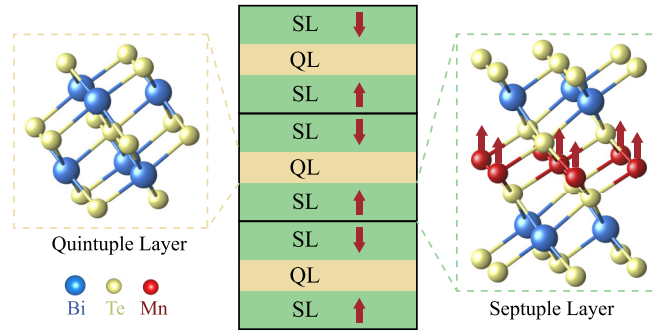

FIG. 2. Schematic illustration of the crystal structures of the AFM $(MnBi_2Te_4)_2(Bi_2Te_3)$ superlattice, where the unit cell consists of a Bi_2Te_3 quintuple layer (QL) sandwiched between two $MnBi_2Te_4$ septuple layers (SLs).

with chiral hinge states between neighboring gapped surface states [20,21], due to the lack of IS and higher-order topology in our system.

Magnetic van der Waals heterostructures. The recently discovered $MnBi_2Te_4$ family of insulators hosts the static axion state with $\theta = \pi$, because the IS is preserved [24]. It is promising to design $(MnBi_2Te_4)_m$-$(Bi_2Te_3)_n$ superlattices, where both $\mathcal{T}$ and $\mathcal{P}$ are broken with suitably chosen m and n, to realize the TI-based dynamical axion state. Here, we take $(MnBi_2Te_4)_2(Bi_2Te_3)$ as a concrete example, also written as $Mn_2Bi_6Te_{11}$. Its crystal structure is schematically shown in Fig. 2. The basic stacking block consists of one Bi_2Te_3 quintuple layer (QL) sandwiched between two $MnBi_2Te_4$ septuple layers (SLs). Based on first-principles calculations, the magnetic structure is the A-type AFM order between nearest SLs and the out-of-plane ferromagnetic order in each SL. The exchange interaction in $Mn_2Bi_6Te_{11}$ is expected to be weaker than that in $MnBi_2Te_4$ due to the intercalation layer Bi_2Te_3.

If ignoring the magnetism, $Mn_2Bi_6Te_{11}$ takes the rhombohedral crystal structure with the same space group D^5_{3d} ($R\bar{3}m$) as Bi_2Te_3. Each atomic layer has a triangular lattice structure, which is stacked in the *ABC* order [24]. The $\mathcal{P}$ is preserved, with the inversion center at the middle Te site of each QL. Once the AFM order is considered, both $\mathcal{T}$ and $\mathcal{P}$ are broken, but their combination $\mathcal{PT}$ is preserved.

The total energies of different magnetic configurations are calculated, shown in Fig. S1 of the Supplemental Material (SM) [73]. The (001)AFM state is found to be the magnetic ground state of $Mn_2Bi_6Te_{11}$. The band structures of the (001)AFM state without and with spin-orbit coupling (SOC) are presented in Figs. 3(a) and 3(b), respectively. The fat band structures demonstrate that the highest valence bands and the lowest conduction bands are dominated by p orbitals of Bi and Te atoms. The SOC induces the "band inversion" between the valence and conduction bands. The inverted band gap is about 0.18 eV, as seen from the density of states shown in Fig. 3(c). Furthermore, in Figs. 3(d) and 3(e), we plot the evolution of the energy gap with gradually tuning the SOC by $\lambda * \lambda_0$, where λ_0 denotes the realistic SOC strength. The energy gap first decreases to a minimum at about $\lambda = 0.68$ [see the inset in Fig. 3(e)] where the "band inversion" occurs, and then increases again. The minimum gap ∼7.6 meV results from the mass term induced by the AFM order.

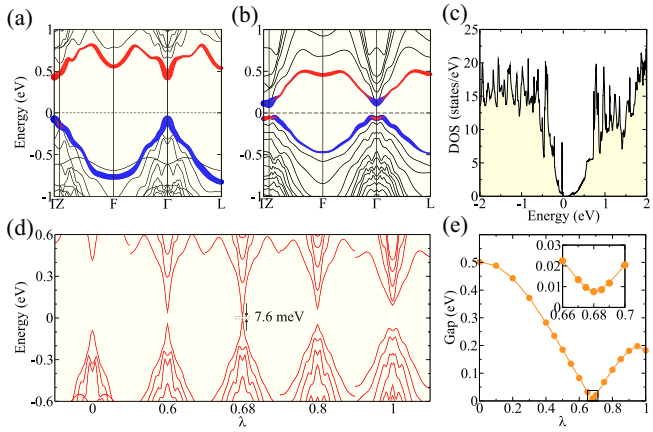

FIG. 3. (a), (b), The band structures (a) without and (b) with SOC. The fat bands indicate a SOC-induced band inversion between p orbitals of Bi (red) and Te (blue) around the Fermi energy. (c) The density of states near the Fermi energy. (d) The evolution of the band structure with increasing the SOC strength $\lambda * \lambda_0$, where λ_0 denotes the realistic SOC strength. (e) The dependence of the band gap on the SOC strength. Inset: The minimum gap (∼7.6 meV) at about $\lambda = 0.68$.

The electronic structure of $Mn_2Bi_6Te_{11}$ can be captured by the above low-energy effective model, and the detailed parameters are provided in the SM [73], which can be obtained by fitting with band structures from first-principles calculations. The negative value of M describes the inverted band structure. To investigate the surface states of $Mn_2Bi_6Te_{11}$, we employed maximally localized Wannier functions [78,79], shown in Fig. S3(a) [73], where the $MnBi_2Te_4$ SL is chosen as the surface termination. The expected gapped Dirac surface state is clearly seen. We also calculate the Fermi surface in Fig. S3(b) [73], which is consistent with the effective model analysis. When the energy level is increased, k-cubic terms must be taken into account, leading to a triangular Fermi surface, as shown in Fig. S3(c) [73], in contrast to the hexagonal Fermi surface in Bi_2Te_3, since the $\mathcal{T}$ is broken.

$Mn_2Bi_6Te_{11}$ has both inverted bulk bands and gapped surface states, and expects to realize the TI-based dynamical axion state with a hidden pseudospin Chern quantity $\nu = -1$. Moreover, based on the low-energy model, we have explicitly calculated the static part θ_0 [49,73] of the axion field as a function of the SOC strength from $\lambda = 0$ to $\lambda = 1$, as shown by the blue line in Fig. 4(a). Due to the presence of the m_5 term, θ_0 deviates from 0 and π. With increasing the SOC strength, θ_0 continuously changes from near 0 with $M \gg |m_5|$ (NI-based phase) to a large value $\sim\pi$ with $M \ll -|m_5|$ (TI-based phase). A rapid increase of θ_0 is found around the (crossover) transition point near $\lambda = 0.68$ with a minimum gap, which is consistent with the first-principles calculations in Fig. 3(e). Intriguingly, in the presence of AFM fluctuations, the axion field will become dynamical with $\theta = \theta_0 + \delta\theta(\mathbf{x}, t)$, and to linear order, $\delta\theta(\mathbf{x}, t) = \delta m_5/g$, where δm_5 is proportional to the amplitude fluctuation of AFM order along the z direction, and g is the coefficient [49].

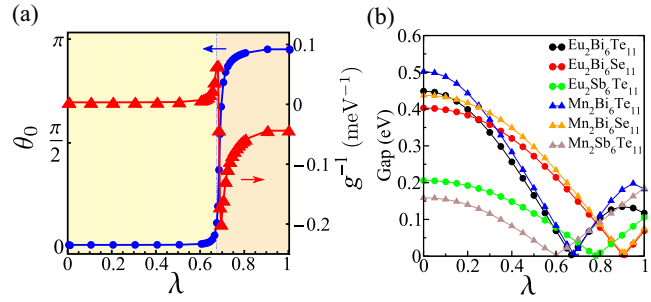

FIG. 4. (a) The evolution of the static part θ_0 of the axion field (blue line) and g^{-1} (red line) of $Mn_2Bi_6Te_{11}$ with tuning the SOC strength λ from 0 to 1, showing a rapid change near the transition point around $\lambda = 0.68$. (b) Evolutions of the energy gap with increasing the SOC strength for this family superlattices of $X_2Y_6X_{11}$ (X = Eu/Mn, Y = Bi/Sb, and Z = Se/Te). Insets of the energy gaps near the minimum point in (b) are shown in Fig. S5 [73].

Discussion. The axion electrodynamics may lead to various exotic physical effects [43,49,54–57], which in turn makes it possible to experimentally detect the dynamical axion field. For example, the axionic polariton, as a collective mode emerging from the coupling between the light and axionic mode, can be detected by the attenuated total reflection measurement [49]. To facilitate the experimental detection of the dynamical axion state, a large proportionality coefficient g^{-1} between $\delta\theta$ and the AFM fluctuation δm_5 is highly preferred. In Fig. 4(a), we plot g^{-1} as a function of the SOC strength for $Mn_2Bi_6Te_{11}$ (see the red line). It clearly shows that the value of g^{-1} in the TI-based side ($M < 0$) is generically one order of magnitude larger than that in the NI-based side ($M > 0$). Notably, g^{-1} becomes significantly large when approaching the transition point from the TI-based side ($M \to 0^-$) [55]. This can be achieved via a chemical replacement by lighter elements with weaker SOC (e.g., Bi by Sb, Te by Se). We present the detailed band structures (see Fig. S4 [73]) and gap evolution with tuning the SOC strength in Fig. 4(b) (insets around minimum energy gaps are shown in Fig. S5 [73]) for the family superlattices $X_2Y_6Z_{11}$ (X = Eu/Mn, Y = Bi/Sb, and Z = Se/Te), some of which are also promising candidates to realize the TI-based dynamical axion state.

Acknowledgments. H.Z. was supported by the National Natural Science Foundation of China (Grants No. 11674165 and No. 11834006), the Fok Ying-Tong Education Foundation of China (Grant No. 161006), the Fundamental Research Funds for the Central Universities (Grant No. 021314380147), and High-Performance Computing Center of Collaborative Innovation Center of Advanced Microstructures. J.W. is supported by the Natural Science Foundation of China through Grant No. 11774065, the National Key Research Program of China under Grant No. 2016YFA0300703, and the Natural Science Foundation of Shanghai under Grants No. 17ZR1442500 and No. 19ZR1471400.

H.W. and D.W. contributed equally to this work.

[1] N. P. Armitage, E. J. Mele, and A. Vishwanath, Rev. Mod. Phys. **90**, 015001 (2018).
[2] X.-L. Qi and S.-C. Zhang, Rev. Mod. Phys. **83**, 1057 (2011).
[3] S. R. Elliott and M. Franz, Rev. Mod. Phys. **87**, 137 (2015).
[4] X.-L. Qi, T. L. Hughes, and S.-C. Zhang, Phys. Rev. B **78**, 195424 (2008).
[5] A. M. Essin, J. E. Moore, and D. Vanderbilt, Phys. Rev. Lett. **102**, 146805 (2009).
[6] G. Rosenberg and M. Franz, Phys. Rev. B **82**, 035105 (2010).
[7] A. Karch, Phys. Rev. Lett. **103**, 171601 (2009).
[8] A. Bermudez, L. Mazza, M. Rizzi, N. Goldman, M. Lewenstein, and M. A. Martin-Delgado, Phys. Rev. Lett. **105**, 190404 (2010).
[9] K. Nomura and N. Nagaosa, Phys. Rev. Lett. **106**, 166802 (2011).
[10] X. Wan, A. Vishwanath, and S. Y. Savrasov, Phys. Rev. Lett. **108**, 146601 (2012).
[11] A. Sekine and K. Nomura, J. Phys. Soc. Jpn. **83**, 104709 (2014).
[12] J. Wang, B. Lian, X.-L. Qi, and S.-C. Zhang, Phys. Rev. B **92**, 081107(R) (2015).
[13] T. Morimoto, A. Furusaki, and N. Nagaosa, Phys. Rev. B **92**, 085113 (2015).
[14] A. M. Turner, Y. Zhang, R. S. K. Mong, and A. Vishwanath, Phys. Rev. B **85**, 165120 (2012).
[15] Z. Wang and S.-C. Zhang, Phys. Rev. B **87**, 161107(R) (2013).
[16] P. Goswami and B. Roy, Phys. Rev. B **90**, 041301(R) (2014).
[17] Y.-L. Lee, H. C. Park, J. Ihm, and Y.-W. Son, Proc. Natl. Acad. Sci. USA **112**, 11514 (2015).
[18] Y. You, G. Y. Cho, and T. L. Hughes, Phys. Rev. B **94**, 085102 (2016).
[19] B. J. Wieder and B. A. Bernevig, arXiv:1810.02373.
[20] C. Yue, Y. Xu, Z. Song, H. Weng, Y.-M. Lu, C. Fang, and X. Dai, Nat. Phys. **15**, 577 (2019).
[21] Y. Xu, Z. Song, Z. Wang, H. Weng, and X. Dai, Phys. Rev. Lett. **122**, 256402 (2019).
[22] Y. S. Hou and R. Q. Wu, arXiv:1902.03372.
[23] M. M. Otrokov, I. P. Rusinov, M. Blanco-Rey, M. Hoffmann, A. Y. Vyazovskaya, S. V. Eremeev, A. Ernst, P. M. Echenique, A. Arnau, and E. V. Chulkov, Phys. Rev. Lett. **122**, 107202 (2019).
[24] D. Zhang, M. Shi, T. Zhu, D. Xing, H. Zhang, and J. Wang, Phys. Rev. Lett. **122**, 206401 (2019).
[25] J. Li, Y. Li, S. Du, Z. Wang, B.-L. Gu, S.-C. Zhang, K. He, W. Duan, and Y. Xu, Sci. Adv. **5**, eaaw5685 (2019).
[26] S. Chowdhury, K. F. Garrity, and F. Tavazza, npj Comput. Mater. **5**, 33 (2019).
[27] L. Wu, M. Salehi, N. Koirala, J. Moon, S. Oh, and N. P. Armitage, Science **354**, 1124 (2016).
[28] S. Grauer, K. M. Fijalkowski, S. Schreyeck, M. Winnerlein, K. Brunner, R. Thomale, C. Gould, and L. W. Molenkamp, Phys. Rev. Lett. **118**, 246801 (2017).
[29] M. Mogi, M. Kawamura, A. Tsukazaki, R. Yoshimi, K. S. Takahashi, M. Kawasaki, and Y. Tokura, Sci. Adv. **3**, eaao1669 (2017).
[30] K. N. Okada, Y. Takahashi, M. Mogi, R. Yoshimi, A. Tsukazaki, K. S. Takahashi, N. Ogawa, M. Kawasaki, and Y. Tokura, Nat. Commun. **7**, 12245 (2016).
[31] M. Mogi, M. Kawamura, R. Yoshimi, A. Tsukazaki, Y. Kozuka, N. Shirakawa, K. S. Takahashi, M. Kawasaki, and Y. Tokura, Nat. Mater. **16**, 516 (2017).
[32] V. Dziom, A. Shuvaev, A. Pimenov, G. V. Astakhov, C. Ames, K. Bendias, J. Böttcher, G. Tkachov, E. M. Hankiewicz, C. Brüne, B. H., and L. Molenkamp, Nat. Commun. **8**, 15197 (2017).
[33] D. Xiao, J. Jiang, J.-H. Shin, W. Wang, F. Wang, Y.-F. Zhao, C. Liu, W. Wu, M. H. W. Chan, N. Samarth, and C.-Z. Chang, Phys. Rev. Lett. **120**, 056801 (2018).
[34] N. Varnava and D. Vanderbilt, Phys. Rev. B **98**, 245117 (2018).
[35] Y. Gong, J. Guo, J. Li, K. Zhu, M. Liao, X. Liu, Q. Zhang, L. Gu, L. Tang, X. Feng, D. Zhang, W. Li, C. Song, L. Wang, P. Yu, X. Chen, Y. Wang, H. Yao, W. Duan, Y. Xu *et al.*, Chin. Phys. Lett. **36**, 076801 (2019).
[36] B. Chen, F. Fei, D. Zhang, B. Zhang, W. Liu, S. Zhang, P. Wang, B. Wei, Y. Zhang, Z. Zuo, J. Guo, Q. Liu, Z. Wang, X. Wu, J. Zong, X. Xie, W. Chen, Z. Sun, S. Wang, Y. Zhang *et al.*, Nat. Commun. **10**, 4469 (2019).
[37] M. M. Otrokov, I. I. Klimovskikh, H. Bentmann, D. Estyunin, A. Zeugner, Z. S. Aliev, S. Gass, A. U. B. Wolter, A. V. Koroleva, A. M. Shikin, M. Blanco-Rey, M. Hoffmann, I. P. Rusinov, A. Y. Vyazovskaya, S. V. Eremeev, Y. M. Koroteev, V. M. Kuznetsov, F. Freyse *et al.*, Nature (London) **576**, 416 (2019).
[38] X. Gui, I. Pletikosic, H. Cao, H.-J. Tien, X. Xu, R. Zhong, G. Wang, T.-R. Chang, S. Jia, T. Valla, W. Xie, and R. J. Cava, ACS Cent. Sci. **5**, 900 (2019).
[39] M. Allen, Y. Cui, E. Y. Ma, M. Mogi, M. Kawamura, I. C. Fulga, D. Goldhaber-Gordon, Y. Tokura, and Z.-X. Shen, Proc. Natl. Acad. Sci. USA **116**, 14511 (2019).
[40] K. Y. Chen, B. S. Wang, J.-Q. Yan, D. S. Parker, J.-S. Zhou, Y. Uwatoko, and J.-G. Cheng, Phys. Rev. Materials **3**, 094201 (2019).
[41] J. Gooth, B. Bradlyn, S. Honnali, C. Schindler, N. Kumar, J. Noky, Y. Qi, C. Shekhar, Y. Sun, Z. Wang, B. A. Bernevig, and C. Felser, Nature (London) **575**, 315 (2019).
[42] R. D. Peccei and H. R. Quinn, Phys. Rev. Lett. **38**, 1440 (1977).
[43] F. Wilczek, Phys. Rev. Lett. **58**, 1799 (1987).
[44] M. M. Vazifeh and M. Franz, Phys. Rev. B **82**, 233103 (2010).
[45] W.-K. Tse and A. H. MacDonald, Phys. Rev. Lett. **105**, 057401 (2010).
[46] J. Maciejko, X.-L. Qi, H. D. Drew, and S.-C. Zhang, Phys. Rev. Lett. **105**, 166803 (2010).
[47] T. Ochiai, J. Phys. Soc. Jpn. **81**, 094401 (2012).
[48] A. G. Mal'shukov, H. Skarsvåg, and A. Brataas, Phys. Rev. B **88**, 245122 (2013).
[49] R. Li, J. Wang, X.-L. Qi, and S.-C. Zhang, Nat. Phys. **6**, 284 (2010).
[50] J. Wang, R. Li, S.-C. Zhang, and X.-L. Qi, Phys. Rev. Lett. **106**, 126403 (2011).
[51] F. W. Hehl, Y. N. Obukhov, J.-P. Rivera, and H. Schmid, Euro. Phys. J. B **71**, 321 (2009).
[52] J. Wang, B. Lian, and S.-C. Zhang, Phys. Rev. B **93**, 045115 (2016).
[53] J. Wang, C. Lei, A. H. Macdonald, and C. Binek, arXiv:1901.08536.
[54] A. Sekine and K. Nomura, Phys. Rev. Lett. **116**, 096401 (2016).
[55] J. Zhang, D. Wang, M. Shi, T. Zhu, H. Zhang, and J. Wang, arXiv:1906.07891.
[56] H. Ooguri and M. Oshikawa, Phys. Rev. Lett. **108**, 161803 (2012).

[57] T. Imaeda, Y. Kawaguchi, Y. Tanaka, and M. Sato, J. Phys. Soc. Jpn. **88**, 024402 (2019).
[58] L. Fu and C. L. Kane, Phys. Rev. B **76**, 045302 (2007).
[59] S. Coh, D. Vanderbilt, A. Malashevich, and I. Souza, Phys. Rev. B **83**, 085108 (2011).
[60] D. N. Sheng, Z. Y. Weng, L. Sheng, and F. D. M. Haldane, Phys. Rev. Lett. **97**, 036808 (2006).
[61] E. Prodan, Phys. Rev. B **80**, 125327 (2009).
[62] Y. Yang, Z. Xu, L. Sheng, B. Wang, D. Y. Xing, and D. N. Sheng, Phys. Rev. Lett. **107**, 066602 (2011).
[63] R. C. Vidal, H. Bentmann, T. R. F. Peixoto, A. Zeugner, S. Moser, C.-H. Min, S. Schatz, K. Kißner, M. Ünzelmann, C. I. Fornari, H. B. Vasili, M. Valvidares, K. Sakamoto, D. Mondal, J. Fujii, I. Vobornik, S. Jung, C. Cacho, T. K. Kim, R. J. Koch *et al.*, Phys. Rev. B **100**, 121104(R) (2019).
[64] Y. Deng, Y. Yu, M. Z. Shi, J. Wang, X. H. Chen, and Y. Zhang, arXiv:1904.11468.
[65] C. Liu, Y. Wang, H. Li, Y. Wu, Y. Li, J. Li, K. He, Y. Xu, J. Zhang, and Y. Wang, Nat. Mater. (2020), doi: 10.1038/s41563-019-0573-3 (2020).
[66] S. Zhang, R. Wang, X. Wang, B. Wei, B. Chen, H. Wang, G. Shi, F. Wang, B. Jia, Y. Ouyang, F. Xie, F. Fei, M. Zhang, X. Wang, D. Wu, X. Wan, F. Song, H. Zhang, and B. Wang, Nano Lett. **20**, 709 (2020).
[67] H. Sun, B. Xia, Z. Chen, Y. Zhang, P. Liu, Q. Yao, H. Tang, Y. Zhao, H. Xu, and Q. Liu, Phys. Rev. Lett. **123**, 096401 (2019).
[68] R. C. Vidal, A. Zeugner, J. I. Facio, R. Ray, M. H. Haghighi, A. U. B. Wolter, L. T. Corredor Bohorquez, F. Caglieris, S. Moser, T. Figgemeier, T. R. F. Peixoto, H. B. Vasili, M. Valvidares, S. Jung, C. Cacho, A. Alfonsov, K. Mehlawat, V. Kataev, C. Hess, M. Richter, B. Büchner *et al.*, Phys. Rev. X **9**, 041065 (2019).
[69] C. Hu, X. Zhou, P. Liu, J. Liu, P. Hao, E. Emmanouilidou, H. Sun, Y. Liu, H. Brawer, A. P. Ramirez, L. Ding, H. Cao, Q. Liu, D. Dessau, and N. Ni, Nat. Commun. **11**, 97 (2020).
[70] J. Wu, F. Liu, M. Sasase, K. Ienaga, Y. Obata, R. Yukawa, K. Horiba, H. Kumigashira, S. Okuma, T. Inoshita, and H. Hosono, Sci. adv. **5**, eaax9989 (2019).
[71] D. J. E. Marsh, K. C. Fong, E. W. Lentz, L. Šmejkal, and M. N. Ali, Phys. Rev. Lett. **123**, 121601 (2019).
[72] H. Zhang, C.-X. Liu, X.-L. Qi, X. Dai, Z. Fang, and S.-C. Zhang, Nat. Phys. **5**, 438 (2009).
[73] See Supplemental Material at http://link.aps.org/supplemental/10.1103/PhysRevB.101.081109 for the detailed derivation of the pseudospin Chern number, effective surface states, Wilson-loop characterization, and more details of $Mn_2Bi_6Te_{11}$ and other compounds.
[74] H. Li, L. Sheng, D. N. Sheng, and D. Y. Xing, Phys. Rev. B **82**, 165104 (2010).
[75] R. Yu, X. L. Qi, A. Bernevig, Z. Fang, and X. Dai, Phys. Rev. B **84**, 075119 (2011).
[76] B. A. Bernevig, T. L. Hughes, and S.-C. Zhang, Science **314**, 1757 (2006).
[77] B. A. Bernevig and T. L. Hughes, *Topological Insulators and Topological Superconductors* (Princeton University Press, Princeton, NJ, 2013).
[78] N. Marzari and D. Vanderbilt, Phys. Rev. B **56**, 12847 (1997).
[79] H.-J. Zhang, C.-X. Liu, X.-L. Qi, X.-Y. Deng, X. Dai, S.-C. Zhang, and Z. Fang, Phys. Rev. B **80**, 085307 (2009).